

Surrogate Quantum Circuit Design for the Lattice Boltzmann Collision Operator

Monica Lăcătuș^{*1}, Matthias Möller¹

Abstract

Direct numerical simulation of turbulent flows at high Reynolds numbers remains a major challenge for traditional computational fluid dynamics (CFD) tools running on classical computer hardware. This has motivated growing interest in quantum algorithms for CFD to enable flow simulations on quantum computers. The reason being that these computers are expected to deliver potential speed-ups for certain problems. One promising quantum CFD approach is a fully quantum implementation of the lattice Boltzmann method called QLBM. Although efficient quantum routines are now available for the streaming step, implementing the nonlinear, irreversible collision step with a low depth circuit that avoids additional ancilla qubits, probabilistic post-selection and repeated executions remains a significant challenge. In this study, we address this challenge by introducing a framework for learning a surrogate quantum circuit (SQC) that approximates the full Bhatnagar–Gross–Krook (BGK) collision operator for the D_2Q_9 lattice. The four-qubit circuit is trained to respect the physical properties of the BGK collision operator, including mass and momentum conservation, D_8 equivariance and scale equivariance. When compiled to the gate set used by IBM’s Heron processor under the assumption of full qubit connectivity, the 15-block SQC requires only 2,430 native gates and uses neither ancilla qubits nor post-selection or repeated executions. Moreover, its depth is independent of the grid resolution, as collision is a local operation that can exploit quantum parallelism to its full extent. We validate the SQC on two benchmark flows, the Taylor–Green vortex decay and the lid-driven cavity, demonstrating that it accurately captures vortex dissipation and flow recirculation. To our knowledge, this is the lowest-depth quantum approximation of the BGK operator reported to date, and it establishes the foundation for scalable QLBM simulations.

1. Introduction

Despite decades of study, turbulence remains a central challenge in fluid mechanics, both numerically and theoretically. Turbulent fluctuations span a

¹Delft Institute of Applied Mathematics, Delft University of Technology, Mekelweg 4, 2628 CD Delft, The Netherlands, Corresponding author*: m.i.l.lacatus@tudelft.nl, Contributing author: m.moller@tudelft.nl

large range of length and time scales, differing by several orders of magnitude. The grid resolution and time-step refinement required for accurate simulations increase steeply with the flow Reynolds number (Re). In practice, the total number of degrees of freedom in a direct numerical simulation (DNS) scale roughly as Re^3 , meaning that fully resolving the flow field has, to date, been feasible only at low- Re numbers and for simple, canonical geometries [1, 2]. This limitation arises not only from the sheer number of arithmetic operations but also from the prohibitive memory demands of storing high-fidelity fields throughout the simulation. Moreover, as the historic pace of Moore’s Law is predicted to slow down [3], the gap between available classical hardware performance and the requirements of high- Re DNS continues to widen. This has prompted growing interest in alternative computing paradigms such as quantum computing.

Quantum computers exploit superposition and entanglement to perform certain tasks more efficiently than classical computers. For example, Shor’s algorithm computes integer factorization in polynomial time [4], and Grover’s algorithm searches unsorted databases with a quadratic speedup [5]. Both algorithms thus demonstrate proven theoretical advantages over the best-known classical methods. Nevertheless, present quantum devices remain in the noisy intermediate-scale quantum (NISQ) era, with limited qubit counts and shallow circuit depths that preclude their use in real engineering applications. Nevertheless, ongoing developments in hardware design and error-mitigation techniques are steadily improving their reliability [6]. Once quantum hardware reaches a mature, fault-tolerant stage, its primary value will be in solving problems that classical computers struggle with. This potential has fueled sustained interest in developing quantum algorithms for computational fluid dynamics (QCFD) aimed at overcoming current limitations in resolving turbulence at high- Re numbers. Broadly speaking, these algorithms fall into three categories: methods that seek to solve the Navier–Stokes equations directly [7–11], quantum lattice-gas cellular automata (LGCA) simulations [12–16] and quantum versions of the lattice Boltzmann method (LBM). In this work, we focus exclusively on the latter.

Classically, LBM operates at the mesoscopic level, recovering the Navier–Stokes equations in the weakly compressible limit by streaming and colliding particle distribution functions on a discrete lattice. Unlike the Navier–Stokes formulation, in which nonlinearity and non-locality are coupled by the convection term, LBM decouples these effects. The linear streaming step performs non-local transport, while the collision step handles local, nonlinear relaxation of the distributions toward equilibrium. This separation makes LBM inherently parallelizable, and GPU-accelerated implementations have demonstrated speedups of one-to-two orders of magnitude over traditional Navier–Stokes solvers on benchmark cases [17]. The same parallelism suggests a natural fit for quantum computing, since encoding the distribution functions into superposed quantum registers would allow a quantum implementation of the LBM to update an exponentially large configuration in the same number of steps required classically for a single configuration.

However, the development of an end-to-end quantum LBM (QLBM) algorithm

has thus far encountered a major bottleneck. The collision step in LBM is both nonlinear and irreversible. These features conflict with the unitarity requirement of quantum operations, which must be linear and reversible. Consequently, early QLBM research has focused exclusively on the streaming step. Todorova and Steijl [18] implemented this transport as a quantum walk using multiple controlled-NOT (CNOT) gates. Schalkers and Möller [19] later reduced the total number of CNOTs and introduced an object-encoding scheme with robust boundary conditions in their Quantum Transport Method (QTM). In subsequent work [20], they developed an efficient technique for computing observables, such as the force acting on an object, by using a quantum version of the momentum-exchange method from classical LBM simulations.

In recent years, various algorithms have been developed to implement the collision step in a QLBM simulation. Many of these algorithms truncate the equilibrium distribution at first order in the macroscopic velocity, thereby discarding the quadratic nonlinear terms in the velocity [21–23]. The result is a fully linear collision operator such that the full Navier–Stokes equations can no longer be recovered. This confines QLBM to low-Re number regimes. Moreover, although the collision operator is linear, it remains non-unitary. The common solution is to use the linear combination of unitaries (LCU) technique [24]. With LCU, a non-unitary matrix can be implemented as a weighted sum of unitaries. This, however, comes at the cost of an extra ancilla qubit and the need to perform mid-circuit measurement and post-selection on the ancilla qubit. Since post-selection succeeds only probabilistically, each QLBM time step may require re-initializing and repeating the circuit several times until the desired outcome is obtained. This severely undermines any quantum advantage of a QLBM simulation over a classical LBM simulation, especially for long simulation times where the success probability reduces with each additional time step.

Kumar and Frankel [25] follow a slightly different approach and express the QLBM algorithm as a matrix–vector product. The vector represents the distribution functions, and the matrix represents the linear collision and streaming operators. As this matrix is non-unitary, they perform classical singular-value decomposition to break it down into a sum of unitary matrices that can be simulated using LCU. The main advantage of their algorithm is that, compared to earlier implementations of LCU, the number of unitaries needed is fixed (eight per time step) and does not depend on the problem size. Nevertheless, when these unitaries are decomposed into elementary gates, it results in a larger circuit depth of $O(10^5)$ per time step.

Xu et al. [26] propose an ancilla-free algorithm for the D_1Q_3 and D_2Q_5 lattices that uses only two registers, d and q , and implements the linear collision as a series of local unitary operations. This greatly reduces resource requirements compared to the LCU approach. However, the algorithm remains probabilistic and is driven by measurements on register q . A successful outcome on q collapses d into the correctly normalized state for the next iteration, while a failed outcome simply re-runs the same constant-depth circuit on (q, d) . Since each re-run does not require re-encoding d , the algorithm is significantly less costly than LCU-based methods.

Alternative algorithms use Carleman linearization to handle the nonlinear collision by introducing a new variable for each monomial in the equilibrium distribution, resulting in a linear but infinite-dimensional system. Itani and Succi [27] map each monomial into a bosonic Fock space and truncate the expansion at a chosen total occupation number, discarding all higher order terms. This creates a trade-off between accuracy and qubit count. They show that both collision and streaming can then be implemented unitarily, with qubit requirements scaling only logarithmically in the Re number. However, a complete circuit design has yet to be demonstrated, and the method is still limited to low-Re number regimes. Sanavio and Succi [28] instead assemble the truncated collision into a global relaxation matrix and simulate it via an LCU-based approach. This results in a very deep circuit on the order of 10^4 layers. To reduce circuit depth, Sanavio et al. [29] apply block-encoding techniques for sparse operators to embed both collision and streaming into a single unitary. While this lowers the circuit depth, their algorithm still relies on ancilla post-selection, with the overall success probability falling off as the inverse of the fourth power of the number of discrete velocities.

A hybrid approach introduced by Wang et al. [30] replaces the LBM collision with the linear and reversible collision operator used in LGCA simulations. They demonstrate accurate simulations of vortex pair merging and decaying turbulence at higher Re numbers than previous works, but their method requires an expensive corrective step at each iteration to maintain near equilibrium, which denies any quantum advantage. Therefore, developing a unitary collision operator that preserves at least part of the classical collision’s nonlinear, irreversible dynamics, eliminates probabilistic post-selection (and the associated measurements and re-initializations) at each time step, and requires only a low-depth circuit implementation remains an open challenge.

In this work, we address the challenge by classically training a surrogate quantum circuit (SQC) to carry out the collision step. Specifically, we focus on the Bhatnagar–Gross–Krook (BGK) collision operator on the D_2Q_9 lattice, although the method extends readily to other lattices and collision models. Once trained, the SQC can be integrated into the QLBM framework of Schalkers and Möller [19] to enable full end-to-end QLBM simulations. To ensure physical fidelity, we embed mass conservation, momentum conservation, scale equivariance and D_8 equivariance into both the circuit architecture and the learning objective. This design encourages the SQC to approximate the classical BGK collision operator faithfully. Our approach draws inspiration from Corbetta et al. [31], who trained a classical neural network to learn the BGK operator. Training is carried out within a modified version of the quantum circuit learning (QCL) framework introduced by Mitarai et al. [32], which is known to approximate complex functions with minimal circuit depth. The resulting SQC is a low-depth circuit that requires no additional ancilla qubits, no post-selection and no repeated executions, making it a practical building block for scalable QLBM simulations. The remainder of this paper is organized as follows. Section 2 provides background on LBM, summarizes the BGK collision operator’s key properties and reviews the QCL framework. Section 3 details our SQC design choices. Section 4 presents the training results. Section 5 evaluates performance

on two benchmark cases. Finally, Section 6 offers concluding remarks.

2. Background and Theory

In this section we cover the theoretical background that our study is based on. We start with a short overview of the Lattice Boltzmann Method (LBM) and focus primarily on its collision process. Readers seeking a more comprehensive overview of LBM may refer to [33]. We then introduce the fundamentals of quantum circuit learning (QCL) and explain how we will use QCL to learn a surrogate quantum circuit (SQC) for the LBM collision operator. We assume that readers already have a working knowledge of quantum computing principles and standard operations. For a more detailed introduction to these topics please refer to [34].

2.1. The Lattice Boltzmann Method

The LBM is a mesoscopic fluid-simulation technique in which a set of discrete-velocity distribution functions $f_i(\mathbf{x}, t)$, often called particle populations, evolve on a Cartesian lattice in space and time. Each population f_i represents the probability density of particles moving with one of the discrete velocities \mathbf{e}_i . In two dimensions, the most common lattice is based on the D_2Q_9 stencil. This stencil consists of nine populations with nine corresponding discrete velocities: a resting state $\mathbf{e}_0 = (0, 0)$, four axis-aligned velocities $\mathbf{e}_{1...4} = (\pm 1, 0)$ and $(0, \pm 1)$, and four diagonal velocities $\mathbf{e}_{5...8} = (\pm 1, \pm 1)$. At each time step Δt , the method proceeds in two stages:

1. **Streaming:** Each population propagates from its current lattice node \mathbf{x} to the neighboring node at $\mathbf{x} + \mathbf{e}_i \Delta t$:

$$f_i(\mathbf{x}, t) \longrightarrow f_i(\mathbf{x} + \mathbf{e}_i \Delta t, t + \Delta t). \quad (1)$$

2. **Collision:** Populations at each lattice node relax toward the local equilibrium distribution $f_i^{\text{eq}}(\mathbf{x}, t)$, according to a collision operator Ω :

$$f_i(\mathbf{x} + \mathbf{e}_i \Delta t, t + \Delta t) - f_i(\mathbf{x}, t) = \Omega[f_i(\mathbf{x}, t)]. \quad (2)$$

The simplest collision operator is the Bhatnagar–Gross–Krook (BGK) operator:

$$\Omega_{\text{BGK}}(f_i(\mathbf{x}, t)) = -\frac{1}{\tau} [f_i(\mathbf{x}, t) - f_i^{\text{eq}}(\mathbf{x}, t)], \quad (3)$$

where τ is the relaxation time that governs how quickly the populations approach equilibrium. The kinematic viscosity ν of the fluid is directly related to τ by

$$\nu = c_s^2 \left(\tau - \frac{1}{2} \right), \quad (4)$$

with c_s denoting the lattice speed of sound (for D₂Q₉, $c_s = \frac{1}{\sqrt{3}}$). The equilibrium distribution follows from a second-order Hermite expansion of the Maxwell–Boltzmann distribution:

$$f_i^{\text{eq}}(\mathbf{x}, t) = w_i \rho \left[1 + \frac{\mathbf{u} \cdot \mathbf{e}_i}{c_s^2} + \frac{(\mathbf{u} \cdot \mathbf{e}_i)^2 - c_s^2 |\mathbf{u}|^2}{2 c_s^4} \right]. \quad (5)$$

Here the D₂Q₉ lattice weights are

$$w_i = \begin{cases} \frac{4}{9}, & i = 0, \\ \frac{1}{9}, & i = 1, \dots, 4, \\ \frac{1}{36}, & i = 5, \dots, 8. \end{cases}$$

The macroscopic density ρ and momentum $\rho \mathbf{u}$ are obtained from the zeroth and first moments of the distributions:

$$\rho = \sum_{i=0}^8 f_i(\mathbf{x}, t), \quad \rho \mathbf{u} = \sum_{i=0}^8 f_i(\mathbf{x}, t) \mathbf{e}_i. \quad (6)$$

A Chapman–Enskog expansion shows that, in the continuum limit, the LBM recovers the weakly compressible Navier–Stokes equations.

In this study we focus on the BGK collision operator and seek to learn an accurate surrogate quantum circuit for it. To achieve this, our surrogate must have the same properties as the BGK operator. Although a full overview appears in Corbetta et al. [31], we summarize these properties below to motivate and guide our construction of the quantum surrogate.

2.2. Properties of the BGK Operator

2.2.1. D₈ Equivariance

The ability of LBM to recover the weakly compressible Navier–Stokes equations relies on choosing a lattice whose discrete velocities and weights enforce full rotational invariance of both second- and fourth-order moments. This invariance ensures that the pressure tensor and the viscous stress tensor are isotropic. In two dimensions, the D₂Q₉ stencil achieves this by being invariant under the dihedral group D₈, the full symmetry group of a square. D₈ is generated by a 90° rotation r about the origin and a reflection s across one of the square’s symmetry axes (vertical, horizontal, or diagonal). These transformations permute the nine discrete velocity vectors among themselves. Every element of D₈ can be written as r^k or $r^k s$ for $k = 0, 1, 2, 3$, giving the eight group elements

$$D_8 = [I, r, r^2, r^3, s, rs, r^2s, r^3s]. \quad (7)$$

Figure 1 illustrates how each symmetry operation permutes the D₂Q₉ velocity directions and their corresponding populations. Both the streaming and collision

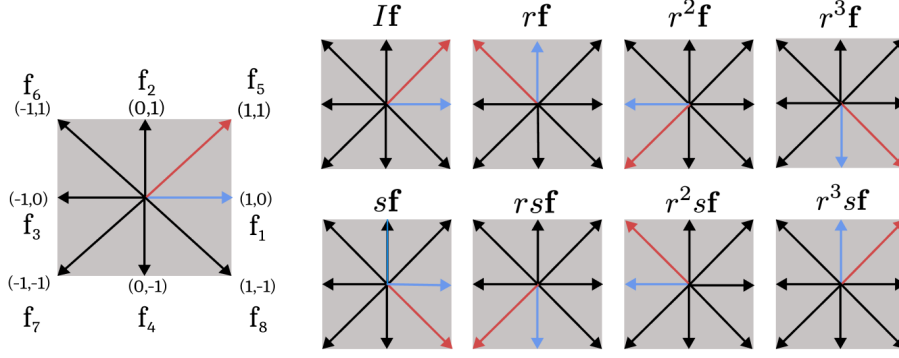


Figure 1: Action of the dihedral group D_8 on the D_2Q_9 populations, showing permutations of the axial f_1 (blue) and diagonal f_5 (red) under each group element. Here r is a 90° anti-clockwise rotation about the origin, and s is a reflection across the horizontal axis.

steps in LBM commute with these permutations. This property is known as D_8 equivariance and be written as follows for the BGK collision

$$\Omega_{\text{BGK}}(\sigma \cdot f_i) = \sigma \cdot \Omega_{\text{BGK}}(f_i), \quad \forall \sigma \in D_8, \quad i = 0, \dots, 8 \quad (8)$$

where $\sigma \cdot f_i$ denotes the permutation of the populations induced by the group element σ .

2.2.2. Scale Equivariance

The BGK collision operator is homogeneous of degree one. This means that if all pre-collision populations are scaled by the same positive factor $\lambda > 0$, the post-collision populations scale by the same factor:

$$\Omega_{\text{BGK}}(\lambda f_i) = \lambda \Omega_{\text{BGK}}(f_i), \quad \forall \lambda > 0, \quad i = 0, \dots, 8 \quad (9)$$

This property ensures that a change of units (lattice units, SI units, etc.) when computing the magnitudes of the pre-collision populations does not affect the magnitudes of the post-collision populations.

2.2.3. Mass and Momentum Invariance

The BGK collision operator exactly conserves mass and momentum. Denoting the post-collision populations by f_i^* , the following thus holds:

$$\sum_{i=0}^8 (f_i^* - f_i) = 0, \quad \sum_{i=0}^8 (f_i^* - f_i) \mathbf{e}_i = \mathbf{0}. \quad (10)$$

2.3. Quantum Circuit Learning

Quantum Circuit Learning (QCL) is a hybrid classical-quantum framework first proposed by Mitarai et al. [32]. In QCL, each input x_i is encoded into a low-depth parametrized quantum circuit $U(x_i, \theta)$ with parameters θ . After applying

the circuit, the expectation value of a chosen observable O is measured. A classical function $F(\{\langle O(x_i, \theta) \rangle\})$ then produces the predicted output $y_i = y(x_i, \theta)$. A classical optimizer adjusts the parameters θ to minimize a loss function $L(h(x_i), y(x_i, \theta))$, where $h(x_i)$ is the target function.

A typical parameterized circuit alternates layers of single-qubit rotation gates with layers of CNOT gates. A rotation on a single qubit about axis (x , y , or z) is defined by

$$U_n(\theta) = \exp\left(-i\frac{\theta}{2}\sigma_n\right), \quad (11)$$

where σ_n is the corresponding Pauli operator (σ_x , σ_y , or σ_z). Applying such rotations in parallel to all N qubits introduces N continuous free parameters per layer. Each qubit is independently mapped to a chosen point on its Bloch sphere, determined by its individual rotation angle and axis. After this layer, the global state becomes a tensor product of N single-qubit states. A subsequent layer of CNOT gates then entangles the qubits by flipping each target qubit whenever its control qubit is in state $|1\rangle$. This operation introduces correlations that cannot be expressed as a simple product state. By repeating these rotation and entangling layers one obtains a universal gate set, meaning that any multi-qubit unitary operation can be approximated to arbitrary precision using only these two gate types.

In practice, however, the precision of such approximations is constrained by the trainability of the circuits. Increasing circuit depth or the number of qubits often leads to regions known as barren plateaus, characterized by gradients that vanish exponentially with system size or depth, as demonstrated by McClean et al. [35]. To avoid these plateaus, one must use few qubits and use a shallow but expressive circuit that incorporates the symmetries of the problem [36]. Under these conditions, QCL offers a promising avenue for learning a unitary approximation of the BGK collision operator. We refer to this approximation as a surrogate quantum circuit (SQC) to emphasize that it does not reproduce the exact BGK collision but instead serves as a quantum approximation of it that can be integrated into the existing QLBM framework.

3. Surrogate Quantum Circuit Design

In this section, we provide a detailed construction and training framework for the surrogate quantum circuit (SQC), designed to model the BGK collision operator on the D_2Q_9 lattice. The SQC is trained to map the nine pre-collision populations $\{f_i\}_{i=0}^8$ to the post-collision populations $\{\hat{f}_i^*\}_{i=0}^8$ so that \hat{f}_i^* closely approximate the true BGK outputs f_i^* . We construct the trainable circuit architecture $U_{\text{SQC}}(\{f_i\}_{i=0}^8, \theta)$ to satisfy the BGK collision invariances and equivariances. Embedding these conservation laws and symmetries into the circuit both enhances its expressivity and mitigates barren plateaus. The following sections describe the quantum state encoding procedure, the SQC architecture, the training protocol, and the evaluation methods used for its validation.

3.1. Quantum State Encoding

To encode the pre-collision population into the quantum state, we use a modified version of the rooted-density encoding introduced in [20], which is also used in the QLBM framework. Since the collision operator acts locally and is thus independent of the lattice positions, we omit any positional qubits when training the SQC. The encoding thus reduces to

$$|\psi_{\text{in}}\rangle = \frac{1}{\sqrt{\sum_{i=0}^8 f_i}} \sum_{i=0}^8 \sqrt{f_i} |\mathbf{e}_i\rangle \quad (12)$$

where the four qubits that are used to encode the discrete velocities \mathbf{e}_i span a 16-dimensional Hilbert space. Nine of the computational basis states encode the discrete velocities \mathbf{e}_i , and the remaining seven basis states are left unoccupied (initialized to zero amplitude). By using only four qubits to encode the pre-collision populations, we significantly reduce the risk of encountering barren plateaus during training. Table 1 gives the full mapping from discrete velocities to four-qubit basis states.

Table 1: Mapping of the nine discrete lattice velocities \mathbf{e}_i into four-qubit basis states.

Population f_i	Discrete Velocity (u_x, u_y)	Velocity Basis State $ Q_3 Q_2 Q_1 Q_0\rangle$
f_0	(0, 0)	0000⟩
f_1	(1, 0)	0001⟩
f_2	(0, 1)	0010⟩
f_3	(−1, 0)	0100⟩
f_4	(0, −1)	1000⟩
f_5	(1, 1)	0011⟩
f_6	(−1, 1)	0110⟩
f_7	(−1, −1)	1100⟩
f_8	(1, −1)	1001⟩

As already discussed in Section 2.2.1, the D_2Q_9 stencil is invariant under the dihedral group D_8 . The eight rotations and reflections that constitute D_8 (see eq. 7) act by permuting the discrete lattice velocities. Because each velocity is mapped onto a computational basis state of four qubits, every symmetry element $\sigma \in D_8$ is realized on the four-qubit register by a unitary U_σ that permutes those qubits exactly as σ permutes the velocities. For example, a 90° physical rotation is implemented as the cyclic permutation of the four qubits by the unitary U_r . A physical reflection across a chosen axis is implemented as a swap of one specific pair of qubits that leaves the other two unchanged by the unitary U_s . Figure 2 illustrates this arrangement where the symmetries of the problem are visualized by placing the four qubits at the corners of a square. The square symmetry of the D_2Q_9 stencil is thus replicated in Hilbert space through the square arrangement of the qubits.

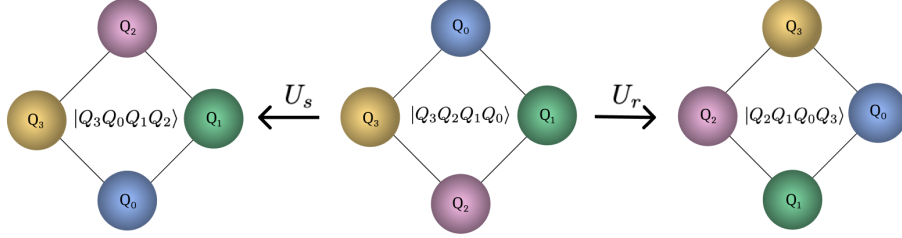


Figure 2: Mapping of lattice symmetries to permutations of qubits in the velocity register: (center) the original 4 qubit basis state $|Q_3Q_2Q_1Q_0\rangle$, (left) the reflection induced by U_s across the horizontal axis permutes qubits $3 \leftrightarrow 1$ (leaving 2 and 0 fixed) giving $|Q_1Q_2Q_3Q_0\rangle$, (right) the 90° anti-clockwise rotation induced by U_r cyclically permutes the qubits $0 \rightarrow 1 \rightarrow 2 \rightarrow 3 \rightarrow 0$, giving $|Q_2Q_1Q_0Q_3\rangle$.

To give a concrete example, consider the discrete velocity $(1, 1)$, which we embed as the basis state $|0011\rangle$. Under a 90° rotation, the physical velocity becomes $(-1, 1)$, and embedding it gives $|0110\rangle$. Equivalently, if we start from $|0011\rangle$ and then cyclically permute the four qubits through the unitary U_r that applies the 90° rotation in the Hilbert space, we arrive at $|0110\rangle$ directly. In other words, embedding first and then applying the unitary representation U_r of the rotation, gives the same result as performing a physical rotation first and then embedding. A similar analysis can be made for a reflection operation. This perfect one-to-one correspondence proves that the encoding is equivariant with respect to the D_8 group.

Furthermore, by comparing the encoding in eq. 12 alongside the LBM definition of the macroscopic density in eq. 6, one sees that the denominator used for the normalization of the state is exactly the square root of the fluid density ($\sqrt{\rho} = \sqrt{\sum_{i=0}^8 f_i}$). Because the encoding and the subsequent SQC circuit are realized entirely through unitary operations, the state normalization, and hence the fluid density, is exactly preserved. As a result, mass conservation emerges inherently from our choice of encoding, without imposing any additional constraints at the circuit level.

A subtlety however arises from embedding the nine populations into the 16-dimensional quantum state. Although the seven surplus basis states are initialized with zero amplitude, unitary evolution by the SQC may transfer some amplitude into them. If one were to compute the final density by summing only over the original nine basis states, this leakage would appear as mass loss. To eliminate this artifact, we include all 16 basis states in the density calculation. Equivalently, our approach may be viewed as employing a D_2Q_{16} stencil, in which the additional seven populations act as fictitious populations with zero discrete velocity. They contribute to the total density but do not directly contribute to the momentum computation, since they carry no discrete velocity. In practice, the leakage into these surplus states can still affect the momentum indirectly by reducing the amplitudes on the nine physical states. Therefore, during training we ensure that the amplitude transfer into the surplus states is minimized,

thereby ensuring these fictitious populations remain negligible (see Section 3.2 for further details).

Finally it is important to mention that since unitary operations are homogeneous of degree one, the scale equivariance of the collision is also naturally enforced.

3.1.1. Circuit Architecture Construction

To design an architecture for the SQC that is expressive enough to approximate the BGK collision operator, we embed the operator's equivariances and invariances directly into the circuit architecture. As discussed in the previous section, scale equivariance and mass conservation follow directly from our encoding and the unitarity of quantum operations. Momentum conservation is harder to enforce and is only partially accounted for, a point we explore in more detail in the next section. Finally, we ensure full D_8 equivariance by imposing that every layer of the SQC commutes with each group action:

$$[U_{\text{SQC}}(f_i, \theta), U_\sigma] = 0 \text{ for all } \theta \in \mathbb{R}, \sigma \in D_8, \quad (13)$$

where $U_{\text{SQC}}(f_i, \theta)$ denotes the parametrized SQC architecture and U_σ is the unitary representation of the D_8 group actions. Enforcing this commutation restricts us to two types of layers:

1. **Global single-qubit rotation layers:** Each of these layers applies the same rotation by angle θ about a fixed axis to all four qubits. They are implemented as²

$$U_n(\theta) = \exp(-i\theta/2\sigma_n)^{\otimes 4} \quad (14)$$

where $\sigma_n = \sigma_x$ or σ_z are the single-qubit Pauli operators. Since each qubit is rotated by the same unitary, the global rotation operator $U_x(\theta)$ (or $U_z(\theta)$) commutes with every element of D_8 . Therefore, performing the rotation before or after any U_σ operation produces the same overall transformation. From here on, we denote $U_x(\theta)$ by X and $U_z(\theta)$ by Z to simplify the notation.

2. **Two-qubit Ising gate layers:** Entanglement is introduced with two-qubit Ising gates rather than the conventional CNOTs. A $\text{CNOT}_{q_c \rightarrow q_t}$ uses one qubit q_c as the control and the other q_t as target. If a symmetry operation U_σ swaps these two qubits, then

$$U_\sigma \text{CNOT}_{q_c \rightarrow q_t} U_\sigma^\dagger = \text{CNOT}_{q_t \rightarrow q_c} \neq \text{CNOT}_{q_c \rightarrow q_t}. \quad (15)$$

The CNOT does not commute with U_σ and breaks D_8 -equivariance. By contrast, the Ising gate

²We restrict the global single-qubit rotations to the x and z axes, since any y -axis rotation can be realized by a sequence of x and z rotations and thus would not increase the expressivity of the circuit architecture.

$$U_{nn}(\theta) = \exp\left(-i\frac{\theta}{2}\sigma_n \otimes \sigma_n\right) \quad (16)$$

where $\sigma_n = \sigma_x$ or σ_z are the single-qubit Pauli operators, is symmetric under the exchange of its two tensor factors:

$$U_\sigma(\sigma_n \otimes \sigma_n) U_\sigma^\dagger = \sigma_n \otimes \sigma_n, \quad \forall \sigma \in D_8. \quad (17)$$

A layer of these gates, all with the same angle θ , therefore preserves the equivariance. The only remaining task is to choose which pairs of the four qubits to entangle. It is most intuitive to revisit the picture of the four qubits arranged at the corners of a square, as shown in Figure 3. In order to ensure D_8 -equivariance, the Ising gates may only couple qubit pairs in patterns invariant under the square's eight symmetries. There are exactly two such patterns: axial couplings between nearest neighbors along the edges of the square and diagonal couplings between opposite corners. We therefore define

$$K_{\text{axial,nn}} = \sum_{\langle i,j \rangle_{\text{edge}}} \sigma_{n,i} \sigma_{n,j}, \quad K_{\text{diag,nn}} = \sum_{\langle i,j \rangle_{\text{corner}}} \sigma_{n,i} \sigma_{n,j}, \quad (18)$$

and implement the layers by

$$U_{\text{axial,nn}}(\theta) = \prod_{\langle i,j \rangle_{\text{edge}}} U_{nn}^{(i,j)}(\theta) = \exp\left(-i\frac{\theta}{2} K_{\text{axial,nn}}\right) \quad (19)$$

where the ordered pairs (i,j) in the edge product are exactly the four nearest-neighbor links $\{(0,1), (1,2), (2,3), (3,0)\}$ between the qubits, and

$$U_{\text{diag,nn}}(\theta) = \prod_{\langle i,j \rangle_{\text{corner}}} U_{nn}^{(i,j)}(\theta) = \exp\left(-i\frac{\theta}{2} K_{\text{diag,nn}}\right) \quad (20)$$

where the corner product runs over the two diagonal links $\{(0,2), (1,3)\}$. In each case, all gates share the same rotation angle θ , and because every axial or diagonal coupling is treated identically, these layers ensure D_8 equivariance. From here on, we denote $U_{\text{axial},xx}$ by XX^A , $U_{\text{axial},zz}$ by ZZ^A , $U_{\text{diag},xx}$ by XX^D and $U_{\text{diag},zz}$ by ZZ^D to simplify the notation.

The complete SQC architecture is assembled by alternating the global single-qubit rotations and two-qubit Ising layers described above. The optimal ordering and number of these layers will be investigated in section 4. Once the SQC circuit is applied to the pre-collision state, we directly read out the post-collision state amplitudes \hat{f}_i^* . Therefore, we do not use an observable or a classical post-processing function as is done in the original QCL framework. This ensures that, once integrated into the QLBM framework, the SQC outputs are already in the exact form required for the streaming step, with no additional measurement or re-initialization needed.

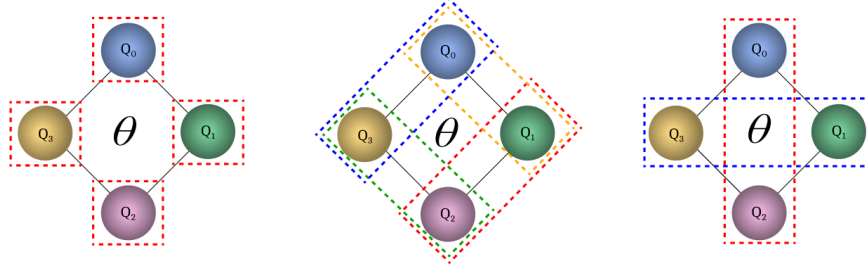


Figure 3: Schematic of the square symmetry of the qubit arrangement and the different ways that qubits can be entangled with each other: (left) qubits are not entangled but they all undergo the same rotation about a chosen axis (x or z) and angle θ , (center) each pair of nearest-neighbor qubits along the edges of the square are entangled and they all undergo a joint rotation about a chosen axis (x or z) and angle θ , (right) qubits on opposite corners of the square are entangled and undergo a joint rotation about a chosen axis (x or z) and angle θ .

3.2. Training Conditions

The SQC is trained on classical hardware using standard mini batch gradient descent. We emphasize that every aspect of training, including all gradient evaluations, is performed entirely on classical processors and thus avoids the extra cost of running the optimization loop on a quantum computer. Training is performed in batches of size $B = 5$, where each sample in the batch is made up of the 9 pre-collision populations f_i and the corresponding nine post-collision populations f_i^* generated using the BGK collision operator. To embed each sample into the full 16-dimensional quantum state space, we append seven all-zero pre- and post-collision populations and encode the resulting 16 populations into the amplitudes of the SQC's input state. We then define a mean-squared-error (MSE) loss between the SQC's predicted post-collision populations \hat{f}_i^* and the ground-truth populations f_i^* from the BGK operator, including all seven zero populations. This ensures that the SQC is trained to minimize the transfer of amplitudes into states that should remain unoccupied. Formally, the loss is

$$\text{MSE} = \frac{1}{(Q+7)B} \sum_{b=1}^B \sum_{i=1}^{Q+7} (f_i^{*(b)} - \hat{f}_i^{*(b)})^2 \quad (21)$$

where $Q = 9$ is the number of populations.

For each training run, we compute an accuracy metric that measures the fraction of post-collision population predictions falling within a prescribed tolerance. Let N be the number of samples in the test (or validation) set, and for each sample n and population index i let $f_i^{*(n)}$ and $\hat{f}_i^{*(n)}$ denote the true and predicted values, respectively. We declare a prediction accurate whenever

$$|f_i^{*(n)} - \hat{f}_i^{*(n)}| < \varepsilon,$$

where the tolerance is chosen as $\varepsilon = 10^{-5}$. Using the indicator function

$$\mathbf{1}\{|f_i^{*(n)} - \hat{f}_i^{*(n)}| < \varepsilon\} = \begin{cases} 1, & \text{if the prediction error is below } \varepsilon, \\ 0, & \text{otherwise.} \end{cases}$$

the average accuracy for population i is simply the fraction of samples whose prediction is accurate within the given tolerance:

$$\langle \text{Accuracy}(f_i) \rangle = \frac{1}{N} \sum_{n=1}^N \mathbf{1}\{|f_i^{*(n)} - \hat{f}_i^{*(n)}| < \varepsilon\}, \quad i = 1, \dots, 9.$$

Since momentum conservation cannot be enforced exactly via the quantum state encoding or the circuit architecture, we add a penalty term to the loss function that quantifies deviations from the exact conservation. For each batch sample b we compute the true momenta

$$p_x^{(b)} = \sum_{i=1}^9 f_i^{*(b)} e_{i,x}, \quad p_y^{(b)} = \sum_{i=1}^9 f_i^{*(b)} e_{i,y} \quad (22)$$

and the predicted momenta

$$\hat{p}_x^{(b)} = \sum_{i=1}^9 \hat{f}_i^{*(b)} e_{i,x}, \quad \hat{p}_y^{(b)} = \sum_{i=1}^9 \hat{f}_i^{*(b)} e_{i,y}. \quad (23)$$

The momentum penalty loss is then defined as

$$L_m = \frac{1}{B} \sum_{b=1}^B \left[(p_x^{(b)} - \hat{p}_x^{(b)})^2 + (p_y^{(b)} - \hat{p}_y^{(b)})^2 \right]. \quad (24)$$

The final loss function combines these terms:

$$L = \text{MSE} + \alpha L_m \quad (25)$$

where α is a regularization weight that increases the relative strength of the momentum penalty over the training iterations.

To ensure the SQC learns the general BGK collision operator rather than biasing toward any single flow case, and to precisely control the ranges and distributions of velocities and densities encountered during training, we generate a fully synthetic dataset following the procedure introduced in [31]. First, we uniformly sample density–velocity pairs (ρ, \mathbf{u}) from $\rho \in [0.95, 1.05]$ and $|\mathbf{u}| \in [0, 0.01]$. For each sample, we compute the equilibrium populations f_i^{eq} via eq. 5. To prevent the pre-collision populations from matching their equilibrium values and thus making the BGK collision step trivial, we introduce non-equilibrium fluctuations. Specifically we compute

$$f_i = f_i^{\text{eq}}(\rho, \mathbf{u}) + f_i^{\text{neq}} \quad (26)$$

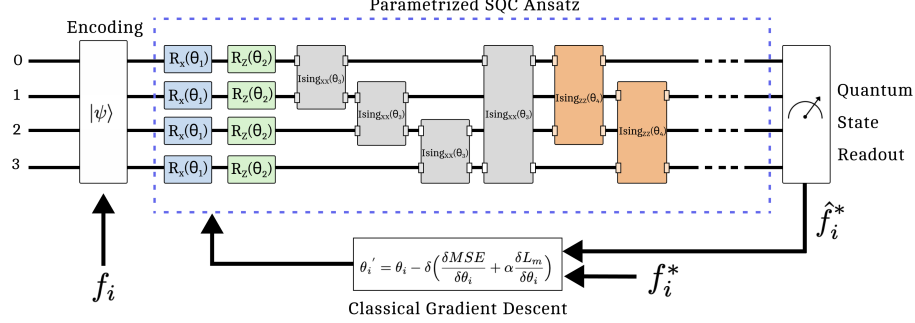


Figure 4: End-to-end training loop for the SQC. Pre-collision populations f_i are encoded into the parametrized circuit, which is executed to obtain the post-collision predictions \hat{f}_i^* . These predictions are evaluated with the combined $MSE + \alpha L_m$ loss, and the circuit parameters θ_i are updated via classical gradient descent.

where each component of f_i^{neq} is drawn from a zero-mean Gaussian distribution with standard deviation $\sigma_{\text{neq}} \in [0, 5 \times 10^{-4}]$. We then apply the BGK collision operator (eq. 2) with a relaxation time $\tau = 1$, to obtain the ground-truth post-collision populations f_i^* . Repeating this procedure $N = 10^6$ times yields a training dataset $\{(f_i, f_i^*)_{i=1}^9\}_{n=1}^N$ that spans the desired density and velocity ranges. A full summary of the settings used for the data generation is given in Appendix A. A schematic of the complete training loop is given in Figure 4.

To efficiently validate the fully trained SQC on meaningful benchmarks, we perform a hybrid quantum–classical simulation in which the collision step is handled by the SQC and the streaming step is performed classically. We assess its performance on two standard LBM test cases: the Taylor–Green vortex decay and the lid-driven cavity flow.

4. Training Results

In this section, we perform several experiments to determine the optimal circuit architecture for the SQC and the best training configuration. Section 4.1 compares several SQC designs to determine which arrangement of single-qubit rotation layers and entangling layers results in the most accurate quantum surrogate for the BGK collision operator. Building on these findings, Section 4.2 presents a circuit depth analysis that quantifies the balance between collision accuracy and total gate count. In Section 4.3, we investigate whether including a momentum penalty in the loss function guides the training towards learning an SQC that better conserves momentum. A complete list of the fixed training parameters used in the above sections is provided in Appendix Sections B to D. Finally, Section 4.4 specifies the SQC architecture and training parameters that we use to benchmark the SQC on the LBM test cases in Chapter 5.

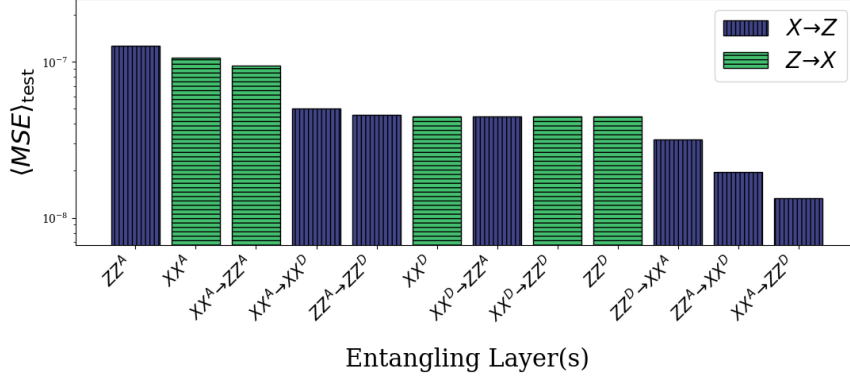


Figure 5: Average test-set MSE loss for each entangling-layer configuration, showing only the rotation-order variant ($X \rightarrow Z$ or $Z \rightarrow X$) that achieved the lowest loss.

4.1. Optimal Circuit Architecture

The number of possible SQC architectures is too large to explore exhaustively, so we focus on designs built from identical blocks that consist of two single-qubit rotation layers (X and Z), and either one or two successive entangling layers drawn from $\{XX^A, XX^D, ZZ^A, ZZ^D\}$. Since X and Z do not commute, the order of the rotation layers matters. We therefore evaluate each design in both orders, $X \rightarrow Z$ and $Z \rightarrow X$. When two entangling layers are included, only the pairs (XX^A, ZZ^D) and (XX^D, ZZ^A) fail to commute. These commutation properties result in exactly 24 distinct circuit blocks for constructing the SQC.

Each architecture is configured to have the same total number of trainable parameters. If one circuit had more free parameters than another, any performance gain might simply reflect its larger number of degrees of freedom rather than the advantages of its gate arrangement or entanglement pattern. To enforce an equal number of parameters, circuits with a single entangling layer use seven repeating blocks, while those with two entangling layers use five blocks plus an additional single-qubit rotation layer at the end. That extra rotation layer restores the missing degree of freedom so that every design, regardless of its entangling-layer count, maintains an identical learning capacity.

For each architecture we carry out three independent training runs and record the average test-set MSE loss without momentum penalization together with the average test-set accuracy for the three representative populations f_0 (rest), f_1 (axial), and f_5 (diagonal). Figure 5 presents, for every entangler configuration, the lower of the two MSE losses obtained under the $X \rightarrow Z$ or $Z \rightarrow X$ rotation orders, arranged from highest loss (left) to lowest loss (right). Figure 6 presents, for each entangler configuration, the higher of the two accuracy values obtained for each of the three populations under the $X \rightarrow Z$ and $Z \rightarrow X$ orders, and arranges the configurations from lowest combined accuracy on the left to highest combined accuracy on the right.

The best performing architecture is the one in which the repeating blocks

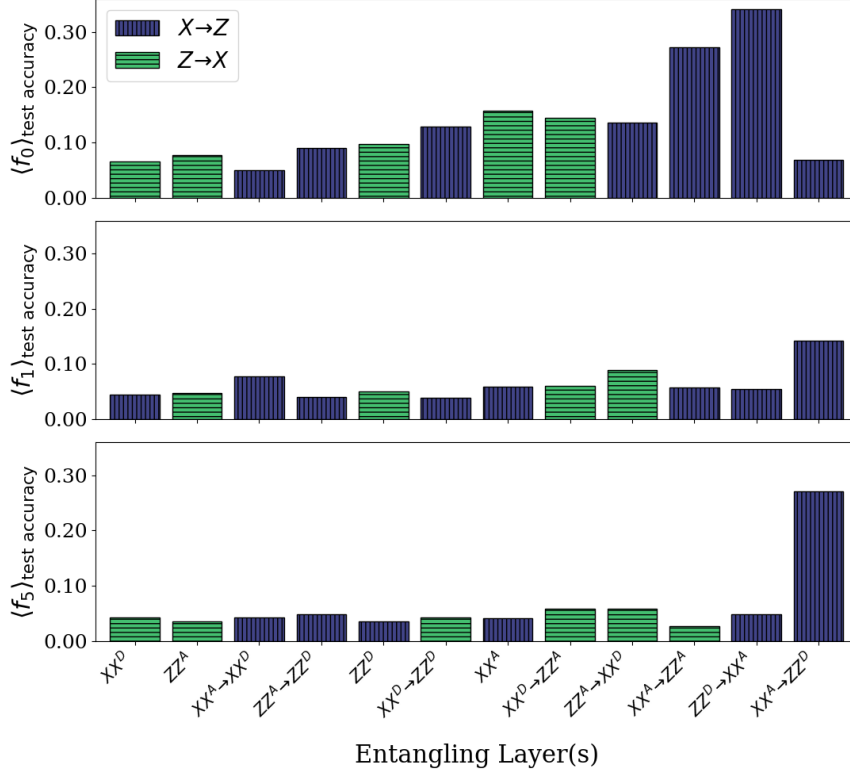


Figure 6: Average test-set accuracy for populations f_0 , f_1 , and f_5 obtained for each entangling-layer configuration. Shown is only the rotation-order variant ($X \rightarrow Z$ or $Z \rightarrow X$) that achieved the highest accuracy.

follow the sequence $\{X, Z, XX^A, ZZ^D\}$. It achieves both the lowest average test-set MSE and the highest combined accuracy across the three populations. We therefore select this SQC architecture for all subsequent training experiments. For reference, this architecture is exactly the one shown in the training loop in Figure 4.

Entangling layer pairs that do not commute (XX^A, ZZ^D) and (XX^D, ZZ^A) show a strong dependence on the order in which they are applied. One ordering increases the accuracy of f_0 at the expense of f_1 and f_5 , and reversing the order inverts that trade-off. This behavior can be understood by examining the equation for the f_0 equilibrium. Since its corresponding discrete lattice velocity is $\mathbf{e}_i = (0, 0)$, the equilibrium is computed according to

$$f_0^{\text{eq}} = w_0 \rho \left[1 - \frac{|\mathbf{u}|^2}{2c_s^2} \right], \quad (27)$$

This functional form differs fundamentally from those of f_1 and f_5 , so the circuit must learn two distinct mappings. Although most architectures score

higher on f_0 , we prioritize f_1 and f_5 because their functional form applies to all other populations. Our chosen SQC architecture indeed results in the best accuracy for those two population.

Architectures with two entangling layers generally outperform those with a single layer, particularly when the layers differ in orientation (one axial and one diagonal) and in type (one XX and one ZZ). Combining different entangling layers in this way, allows these circuits to correlate amplitudes across basis states more effectively and to explore a larger portion of Hilbert space via rotations about multiple axes. Several architectures that achieve high population accuracies do so at the cost of larger MSE losses. Recall that our MSE loss is computed over all 16 basis states (see eq. 21), including those with zero target amplitudes. An architecture can lead to misleading results by transferring amplitude on the seven basis states which should remain unoccupied. This inflates the accuracies of the other 9 basis states while penalizing the MSE loss. Our chosen SQC architecture avoids this trade-off entirely, resulting in both a low MSE loss and high population accuracies.

4.2. SQC Depth Analysis

We evaluate the impact of circuit depth by building SQC variants with 5, 15, and 25 blocks based on the optimal architecture design $\{X, Z, XX^A, ZZ^D\}$. For each circuit depth we conduct three independent training runs. Figure 7a plots the average validation-set MSE loss against training iteration, with values averaged over all runs. Figure 7b shows the average accuracy for all 9 populations, likewise averaged across runs.

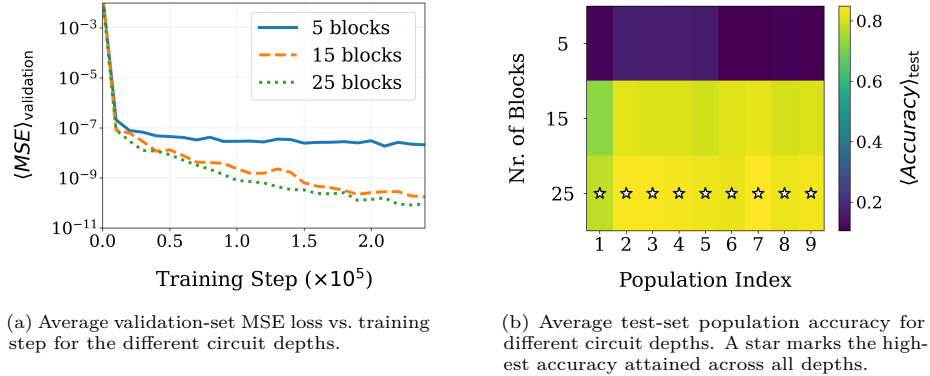


Figure 7: Training results for SQC depth experiments.

These results show that increasing the depth of the circuit both reduces validation loss and improves population accuracies, as one would expect. The gain from 5 to 15 blocks is substantially larger than the gain from 15 to 25 blocks. Each additional block up to a depth of 15 enhances the SQC’s expressivity. Beyond that depth, the gradient norms begin to vanish and barren plateaus appear, causing training to stagnate and preventing further improvement.

The block design relies on gate types that are not all native to current hardware. To get a better idea of the true circuit depth, we decompose each layer into IBM Heron’s native gate set $\{\text{RZ}, \text{SX}, \text{CZ}\}$, where CZ is the only two-qubit gate [37]. This decomposition assumes full all-to-all qubit connectivity and is performed using Qiskit’s transpiler [38]. Table 2 lists the resulting native gate counts for each layer. Because the Ising entangling layers translate primarily into single-qubit RZ and SX operations, the number of two-qubit CZ gates remains minimal.

Table 2: Decomposition of the SQC layers into the IBM Heron native gate set.

Layer	RZ	SX	CZ	Total
X	12	8	0	20
Z	4	0	0	4
XX^A	68	32	8	108
ZZ^D	18	8	4	30

The X and XX^A layers are by far the most expensive to implement, requiring 20 and 108 native gates respectively. This is because for the Z and ZZ^D layers, each arbitrary z -axis rotation maps directly to a RZ native gate. A 25 block circuit needs 4,050 native gates, whereas a 15 block circuit requires only 2,430. Given the minimal performance difference between these depths, we proceed with the 15 block architecture to keep the gate count low. The collision operator acts locally and does not depend on the position register. Therefore, its implementation cost remains constant regardless of the size of the grid. The same 2,430-gate circuit applies at every time step, whether there are 100 grid points or 10^6 grid points. This makes the SQC the shallowest collision circuit proposed to date, which directly models the full BGK operator.

4.3. Momentum Loss Penalization

To evaluate whether the penalty term in the loss function (see eq. 25) guides the training towards learning an SQC that better conserves momentum, we perform a series of training experiments with the penalty enabled. Starting from an initial regularization weight $\alpha = 10^{-4}$, we increase α every 10,000 iterations as follows: in experiment 1 up to $\alpha = 0.25$, in experiment 2 up to $\alpha = 0.5$, in experiment 3 up to $\alpha = 1.0$.

We conduct three independent training runs for each experiment. Figures 8a and 8b show, respectively, the average validation-set MSE loss and the average population accuracy, each computed over the three runs. For comparison, both plots include the 15-block SQC trained without any momentum conservation penalty ($\alpha = 0$) as a baseline.

As we increase the penalty weight from $\alpha = 0$ to $\alpha = 0.5$, the validation-set MSE loss shows a modest decrease throughout training, while test-set accuracy remains essentially unchanged or improves slightly in some populations. Over the same range, the average relative momentum conservation loss on the test-set

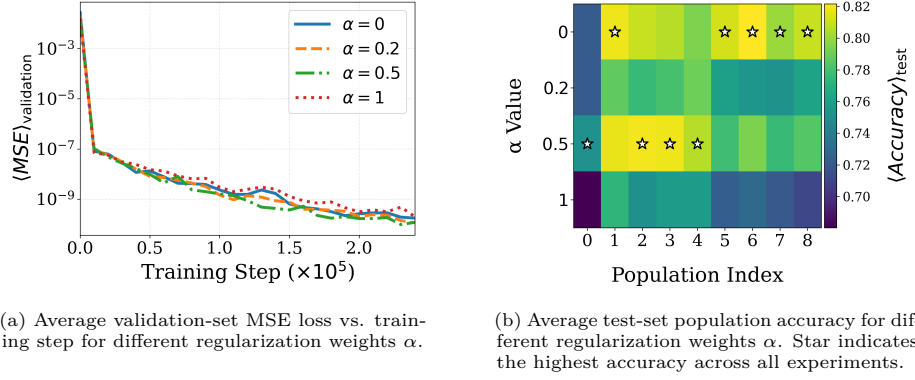


Figure 8: Training results for momentum loss penalty experiments.

drops from 0.0028 at $\alpha = 0$ to 0.0021 at $\alpha = 0.5$. Raising α further to 1.0 continues to lower the momentum loss to 0.0019, but at the cost of increased validation-set MSE loss and noticeably lower accuracy in several populations. This result indicates that a penalty weight of 1.0 overconstrains the learning. Although the SQC which was trained without the penalty terms ($\alpha = 0$) achieves the highest overall accuracy, the configuration with $\alpha = 0.5$ offers the best balance, improving momentum conservation with only a minimal impact on accuracy.

Table 3: Average relative momentum loss on the test-set for different regularization weights α .

α	Average Relative Momentum Loss
0.0	0.0028
0.2	0.0027
0.5	0.0021
1.0	0.0019

4.4. Optimal Training Conditions

Based on the experiments conducted throughout this chapter, we can now specify the best-performing training parameters and architecture for the SQC. These are summarized in Table 4.

5. SQC Evaluation

In this section, we evaluate the SQC collision predictions against those of the classical BGK operator for the Taylor–Green vortex decay in Section 5.1 and the lid-driven cavity flow in Section 5.2. We do not append explicit units to quantities like velocity or time throughout this section because LBM is formulated in dimensionless lattice units.

Table 4: Best-performing SQC training parameters.

Training Parameter	Setting
Architecture	$\{X, Z, XX^A, ZZ^D\}$
Number of block	15
Optimizer	JAX Gradient Descent
Learning Rate	0.05
Training Iterations	750000
Batch Size	5
Momentum Conservation Penalty	ON
Regularization weight (α)	0.5
Parameter Initialization	Uniform on $[-\pi, \pi]$

5.1. Taylor-Green Vortex Decay

The Taylor–Green vortex decay case models vortex dissipation in a fully periodic domain. It serves as a standard benchmark for the incompressible Navier–Stokes equations because it admits an exact Cartesian-coordinate solution. In LBM the streaming step simply propagates populations between neighboring lattice nodes, introducing no physical dissipation beyond minor numerical damping. Vortex decay is therefore driven entirely by the collision operator, which relaxes populations toward the local equilibrium and, in so doing, injects exactly the viscous dissipation that gives rise to the Navier–Stokes viscous-stress tensor in the continuum limit. Without a properly formulated collision step, the flow remains effectively inviscid and the vortices never decay. This makes the Taylor–Green case an ideal validation of any new collision model.

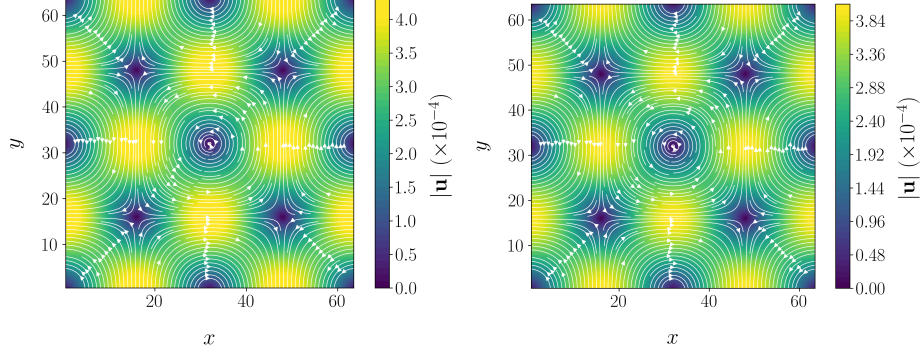
We run two simulations on a two-dimensional periodic grid of size 64×64 lattice nodes. In one simulation the classical BGK operator performs the collision step and in the other the SQC takes that role. Both simulations are initialized with a density equal to $\rho = 1$ and with a velocity field given by:

$$u_x(x, y) = u_0 \sin(k_x x) \cos(k_y y), \quad (28)$$

$$u_y(x, y) = -u_0 \cos(k_x x) \sin(k_y y), \quad (29)$$

with amplitude $u_0 = 0.01$ and wave-numbers $k_x = \frac{2\pi}{64}$, $k_y = \frac{2\pi}{64}$. The Reynolds number for this case is $\text{Re} = 6.3$. We set the relaxation time to $\tau = 1$, and advance each simulation for 1,000 time steps. In the SQC-based simulation we apply the trained circuit at every lattice node independently, embedding the pre-collision distribution into the same 16-dimensional Hilbert space used during training. After each collision step we read out the circuit’s output state to extract the post-collision populations, then carry out the streaming step classically.

Figure 9 displays the velocity magnitude fields at the final time step for both the BGK and SQC collision simulations. The SQC operator closely reproduces the BGK results. The vortices decay at a similar rate and their symmetry is well preserved.



(a) Plot of velocity magnitude for the SQC collision simulation. (b) Plot of velocity magnitude for the BGK collision simulation.

Figure 9: Velocity magnitude and streamlines comparison between the SQC and BGK collision simulations of the Taylor-Green vortex decay case.

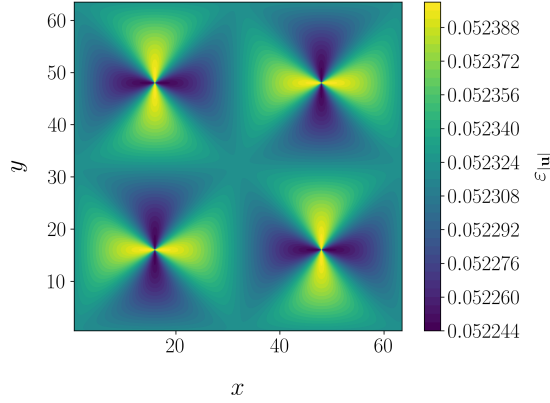
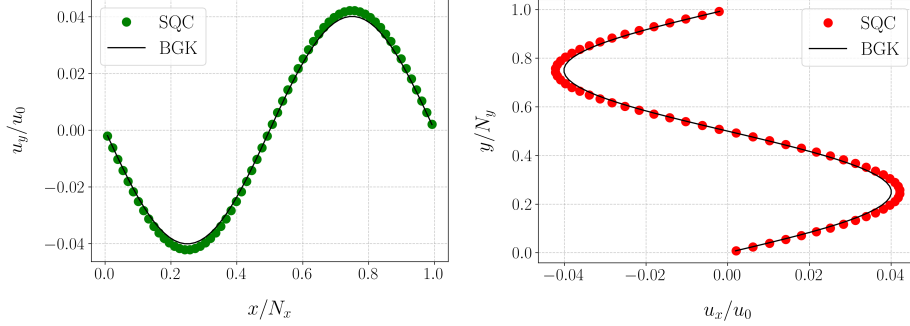


Figure 10: Relative error in velocity magnitude between the SQC and BGK collision simulations of the Taylor-Green vortex decay case.

To better understand the velocity-magnitude error, Figure 10 plots the relative difference between the SQC and BGK velocity magnitudes. The errors are similar throughout the domain and on the order of 0.05. This level of error is acceptable, as the SQC is a unitary approximation and cannot fully capture the BGK operator's nonlinear and irreversible behavior. Figure 11 compares the vertical and horizontal centerline velocities at the domain mid-lines. The match between the centerline velocities is very good, with the SQC only slightly under-predicting the vortex decay and overshooting the BGK peak amplitudes at the extrema. It is important to note that these results were obtained with the 15-block SQC. Using the 25-block SQC would likely improve the agreement further. Overall, these findings demonstrate that a low-depth SQC can model the BGK collision step and provide a good quantum approximation of the classical dynamics.



(a) Centerline profile of the normalized horizontal velocity u_x/u_0 along the domain mid-line. (b) Centerline profile of the normalized vertical velocity u_y/u_0 along the domain mid-line.

Figure 11: Centerline velocities comparison between the SQC and BGK collision simulations of the Taylor-Green vortex decay case.

5.2. Lid-Driven Cavity

The lid-driven cavity flow is a well-known benchmark case. It simulates a fluid enclosed in a square cavity with its top lid moving at a constant speed, driving recirculation within the cavity. We perform two simulations, one using the SQC collision model and one using the BGK operator. The flow Reynolds number is set to $Re = 10$ and we use a 64×64 grid. Bounce-back boundary conditions are used for the no-slip walls, and for the moving lid we impose a bounce-back condition with $u_{lid} = 0.026$. This velocity lies outside the range on which we trained the SQC ($|\mathbf{u}| \in [0.00, 0.01]$). Therefore, this case assesses its ability to extrapolate beyond its training conditions. We initialize the density to $\rho = 1$ and run each simulation for 1,000 time steps.

Figure 12 shows the velocity magnitude plots at the end of the simulations for both the BGK and SQC collision models. A comparison of the two results reveals that the SQC operator reproduces the BGK operator's behavior even when forced to extrapolate. The formation of the large recirculation region within the cavity is captured accurately.

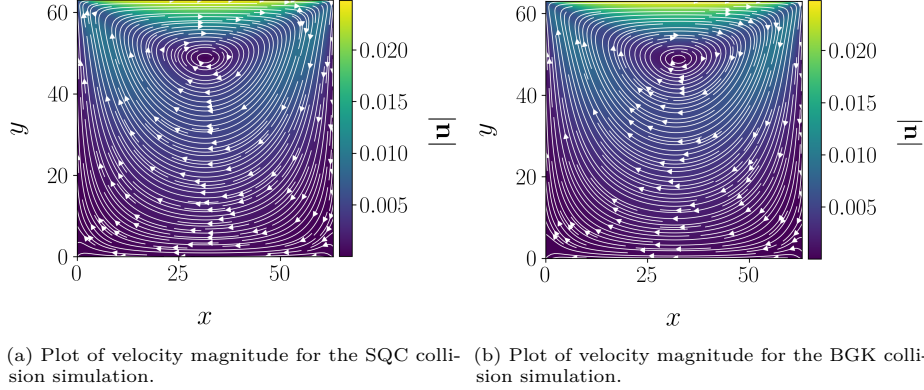


Figure 12: Velocity magnitude and streamlines comparison between the SQC and BGK collision simulations of the lid-driven cavity case.

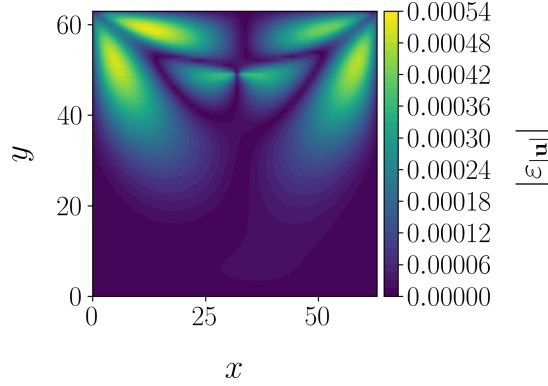
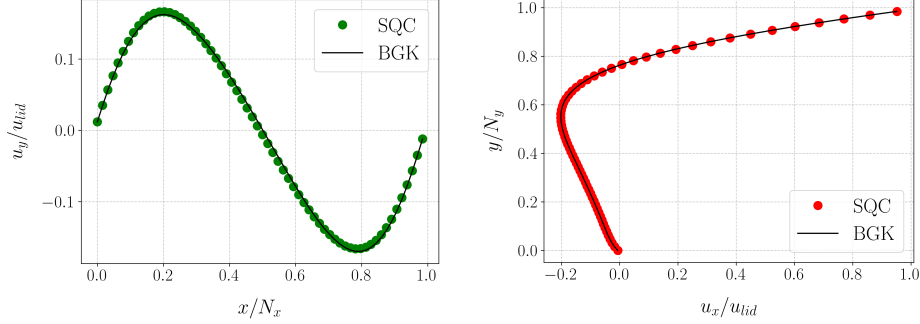


Figure 13: Absolute error in velocity magnitude between the SQC and BGK collision simulations of the lid-driven cavity case.

To better understand the error in velocity magnitude, we plot in Figure 13 the absolute difference between the SQC and BGK simulations. We compare absolute rather than relative error because in regions such as the cavity corners and at the center of the large recirculation zone the flow is nearly stagnant and the velocity is close to zero, which would make any small discrepancy appear large when expressed relatively. The maximum absolute error is on the order of 10^{-4} and is primarily located near the top of the domain where the flow is circulating faster. This error is entirely acceptable given that the SQC is extrapolating outside of its trained velocity range. This is also supported by the near one-to-one match observed for the vertical and horizontal centerline velocities at the domain mid-lines in Figure 14.

Overall, the SQC operator performs very well in both the lid-driven cavity and Taylor–Green vortex decay cases, showing that it accurately reproduces the BGK collision and can even extrapolate beyond its training conditions. It



(a) Centerline profile of the normalized horizontal velocity u_x/u_{lid} along the domain mid-line. (b) Centerline profile of the normalized vertical velocity u_y/u_{lid} along the domain mid-line.

Figure 14: Centerline velocities comparison between the SQC and BGK collision simulations of the lid-driven cavity case..

is important to clarify that at the Re numbers we examined, the nonlinear contributions to the equilibrium distribution are negligible. The collision step is effectively governed by linear dynamics. We therefore do not claim that SQC has captured the full nonlinear structure of the BGK operator. Rather, in this low-Re regime, it has learned an accurate, low-depth approximation of the (irreversible) BGK collision process.

6. Conclusion

In this study, we introduced a novel framework for training an SQC that delivers a low-depth unitary approximation of the BGK collision operator on the D_2Q_9 lattice. By explicitly enforcing mass and momentum conservation, D_8 symmetry, and scale equivariance in the circuit design and training, the SQC faithfully captures the essential physics of the BGK operator. The optimal SQC architecture uses 15 identical blocks, each comprising two layers of single qubit rotations (an X layer followed by a Z layer) and two layers of Ising entanglers (first an axial XX^A layer, then a diagonal ZZ^D layer). When mapped to the native gate set of IBM's Heron processor, assuming full qubit connectivity, this 15-block circuit requires only 2,430 native gates. Although this gate count remains challenging for today's NISQ devices, it is several orders of magnitude lower than earlier quantum collision implementations and eliminates the need for probabilistic post-selection or repeated executions. Moreover, because the collision acts locally at each lattice site, the same circuit may be applied in parallel across an arbitrarily large grid, making the total gate count independent of grid size.

We validated the SQC using two classical benchmark flows. In the Taylor-Green vortex decay case, the circuit reproduces the expected rate of viscous dissipation with only minor deviations from the BGK solution. In the lid-driven cavity flow, accuracy is preserved even when the flow velocity exceeds the

training range, again showing only small discrepancies. In both benchmarks, the SQC’s predictions remain within acceptable error margins relative to reference simulations of the exact BGK operator.

Designing and training the SQC in this way has produced an accurate, low-depth quantum approximation of the classical BGK collision operator, representing an important step towards enabling end-to-end QLBM simulations. Future work will extend the framework to three-dimensional lattices such as D_3Q_{27} , optimize state preparation to reduce resource requirements, integrate the trained circuit into the existing QLBM framework, and explore learned surrogates capable of operating at higher Re numbers.

7. Acknowledgements

We gratefully acknowledge support from the joint research program Quantum Computational Fluid Dynamics by Fujitsu Limited and Delft University of Technology, co-funded by the Netherlands Enterprise Agency under project number PPS23-3-03596728.

References

- [1] Q. Li, P. Schlatter, L. Brandt, D. S. Henningson, DNS of a spatially developing turbulent boundary layer with passive scalar transport, *International Journal of Heat and Fluid Flow* 30 (5) (2009) 916–929. doi:10.1016/j.ijheatfluidflow.2009.06.007.
- [2] J. Yao, S. Rezaeiravesh, P. Schlatter, F. Hussain, Direct numerical simulations of turbulent pipe flow up to $Re_\tau \approx 5200$, *Journal of Fluid Mechanics* 956 (2023) A18. doi:10.1017/jfm.2022.1013.
- [3] T. N. Theis, H.-S. P. Wong, The End of Moore’s Law: A New Beginning for Information Technology, *Computing in Science & Engineering* 19 (2) (2017) 41–50. doi:10.1109/MCSE.2017.29.
- [4] P. W. Shor, Algorithms for Quantum Computation: Discrete Logarithms and Factoring, in: *Proceedings of the 35th Annual Symposium on Foundations of Computer Science (FOCS)*, IEEE, Santa Fe, NM, USA, 1994, pp. 124–134. doi:10.1109/SFCS.1994.365700.
- [5] L. K. Grover, A Fast Quantum Mechanical Algorithm for Database Search, in: *Proceedings of the Twenty-Eighth Annual ACM Symposium on Theory of Computing (STOC ’96)*, 1996, pp. 212–219. doi:10.1145/237814.237866.
- [6] A. Kandala, K. Temme, A. D. Córcoles, A. Mezzacapo, J. M. Chow, J. M. Gambetta, Error mitigation extends the computational reach of a noisy quantum processor, *Nature* 567 (2019) 491–495. doi:10.1038/s41586-019-1040-7.

- [7] F. Gaitan, Finding flows of a Navier–Stokes fluid through quantum computing, npj Quantum Information 6. doi:10.1038/s41534-020-00291-0.
- [8] L. Budinski, Quantum algorithm for the Navier–Stokes equations by using the streamfunction-vorticity formulation and the lattice Boltzmann method, International Journal of Quantum Information 20 (02). doi:10.1142/S0219749921500398.
- [9] Y. Liu, Z. Chen, C. Shu, P. Rebentrost, Y. Liu, S. C. Chew, B. C. Khoo, Y. D. Cui, A variational quantum algorithm–based numerical method for solving potential and Stokes flows, arXiv preprint arXiv:2303.01805.
- [10] Z. Song, R. Deaton, B. Gard, S. H. Bryngelson, Incompressible Navier–Stokes solve on noisy quantum hardware via a hybrid quantum–classical scheme, arXiv preprint arXiv:2406.00280.
- [11] O. Kyriienko, A. E. Paine, V. E. Elfving, Solving nonlinear differential equations with differentiable quantum circuits, arXiv preprint arXiv:2011.10395.
- [12] J. Yepez, Quantum lattice-gas model for the Burgers equation, Journal of Statistical Physics 107 (1-2) (2002) 203–224. doi:10.1023/A:1014514805610.
- [13] A. D. Bastida Zamora, L. Budinski, O. Niemimäki, V. Lahtinen, Efficient quantum lattice gas automata, Computers & Fluids Article 106476. doi:10.1016/j.compfluid.2024.106476.
- [14] N. Fonio, P. Sagaut, G. Di Molfetta, Quantum collision circuit, quantum invariants and quantum phase estimation procedure for fluid dynamic lattice gas automata, Computers & Fluids 299 (2025) 106688. doi:10.1016/j.compfluid.2025.106688.
- [15] M. A. Schalkers, M. Möller, On the importance of data encoding in quantum Boltzmann methods, Quantum Information Processing 23 (1) (2024) 20. doi:10.1007/s11128-023-04216-6.
- [16] P. Love, On Quantum Extensions of Hydrodynamic Lattice Gas Automata, Condensed Matter 4 (2) (2019) 48. doi:10.3390/condmat4020048.
- [17] H. Yu, R. Chen, H. Wang, Z. Yuan, Y. Zhao, Y. An, Y. Xu, L. Zhu, GPU accelerated lattice Boltzmann simulation for rotational turbulence, Computers & Mathematics with Applications 67 (2) (2014) 437–451. doi:10.1016/j.camwa.2013.09.017.
- [18] B. N. Todorova, R. Steijl, Quantum algorithm for the collisionless Boltzmann equation, Journal of Computational Physics 409 (2020) 109347. doi:10.1016/j.jcp.2020.109347.
- [19] M. A. Schalkers, M. Möller, Efficient and fail-safe quantum algorithm for the transport equation, Journal of Computational Physics 502 (2024) Article 112816. doi:10.1016/j.jcp.2024.112816.

- [20] M. A. Schalkers, M. Möller, Momentum exchange method for quantum Boltzmann methods, *Computers & Fluids* 285 (2024) Article 106453. doi:10.1016/j.compfluid.2024.106453.
- [21] M. Lee, Z. Song, S. Kocherla, A. Adams, A. Alexeev, S. H. Bryngelson, A multiple-circuit approach to quantum resource reduction with application to the quantum lattice Boltzmann method, *arXiv preprint arXiv:2401.12248*.
- [22] D. Wawrzyniak, J. Winter, S. Schmidt, T. Indinger, C. F. Janßen, U. Schramm, N. A. Adams, A quantum algorithm for the lattice-Boltzmann method advection-diffusion equation, *Computer Physics Communications* 306 (2024) 109373. doi:10.1016/j.cpc.2024.109373.
- [23] L. Budinski, Quantum algorithm for the advection-diffusion equation simulated with the lattice Boltzmann method, *Quantum Information Processing* 20 (2021) 57. doi:10.1007/s11128-021-02996-3.
- [24] A. M. Childs, N. Wiebe, Hamiltonian Simulation Using Linear Combinations of Unitary Operations, *Quantum Inf. Comput.* 12 (11-12) (2012) 901-924. doi:10.5555/2481569.2481570.
- [25] E. D. Kumar, S. H. Frankel, Quantum unitary matrix representation of the lattice Boltzmann model for low Reynolds fluid flow simulation, *AVS Quantum Science* 7 (1) (2025) 013802. doi:10.1116/5.0245082.
- [26] L. Xu, M. Li, L. Zhang, H. Sun, J. Yao, Improved quantum lattice Boltzmann method for advection-diffusion equations with a linear collision model, *Physical Review E* 111 (4) (2025) 045305. doi:10.1103/PhysRevE.111.045305.
- [27] W. Itani, K. R. Sreenivasan, S. Succi, Quantum Algorithm for Lattice Boltzmann (QALB) Simulation of Incompressible Fluids with a Nonlinear Collision Term, *Physics of Fluids* 36 (1) (2024) 017112. doi:10.1063/5.0176569.
- [28] C. Sanavio, S. Succi, Lattice Boltzmann-Carleman quantum algorithm and circuit for fluid flows at moderate Reynolds number, *AVS Quantum Science* 6 (2) (2024) 023802. doi:10.1116/5.0195549.
- [29] C. Sanavio, W. A. Simon, A. Ralli, P. Love, S. Succi, Carleman-lattice-Boltzmann quantum circuit with matrix access oracles, *Physics of Fluids* 37 (3) (2025) 037123. doi:10.1063/5.0254588.
- [30] B. Wang, Z. Meng, Y. Zhao, Y. Yang, Quantum lattice Boltzmann method for simulating nonlinear fluid dynamics (2025). *arXiv:arXiv:2502.16568*, doi:10.48550/arXiv.2502.16568.
- [31] A. Corbetta, A. Gabbana, V. Gyrya, D. Livescu, J. Prins, F. Toschi, Toward learning lattice Boltzmann collision operators, *European Physical Journal E* 46 (3) (2023) 10. doi:10.1140/epje/s10189-023-00267-w.

- [32] K. Mitarai, M. Negoro, M. Kitagawa, K. Fujii, Quantum circuit learning, *Phys. Rev. A* 98 (3) (2018) 032309, published 10 September 2018. doi:10.1103/PhysRevA.98.032309.
- [33] T. Krüger, H. Kusumaatmaja, A. Kuzmin, O. Shardt, G. Silva, E. M. Viggien, *The Lattice Boltzmann Method: Principles and Practice*, 1st Edition, Graduate Texts in Physics, Springer, 2017. doi:10.1007/978-3-319-44649-3.
- [34] M. A. Nielsen, I. L. Chuang, *Quantum Computation and Quantum Information*, 1st Edition, Cambridge Series on Information and the Natural Sciences, Cambridge University Press, Cambridge, UK, 2000. doi:10.1017/CB09780511976667.
- [35] J. R. McClean, S. Boixo, V. N. Smelyanskiy, R. Babbush, H. Neven, Barren plateaus in quantum neural network training landscapes, *Nature Communications* 9 (2018) 4812, published 16 November 2018. doi:10.1038/s41467-018-07090-4.
- [36] Q. T. Nguyen, L. Schatzki, P. Braccia, M. Ragone, P. J. Coles, F. Sauvage, M. Larocca, M. Cerezo, Theory for Equivariant Quantum Neural Networks, *PRX Quantum* 5 (2024) 020328, published 6 May 2024. doi:10.1103/PRXQuantum.5.020328.
- [37] IBM Quantum, Native gates and operations, IBM Quantum Documentation, 2017–2025. [Online; accessed Jul. 4, 2025] (2025).
- [38] IBM Quantum, Transpiler, IBM Quantum Documentation, <https://quantum.cloud.ibm.com/docs/en/api/qiskit/transpiler> (accessed July 14, 2025) (2025).

Appendices

A. Data Generations

Table 5: Parameters used in data generation.

Parameter	Symbol	Value
Number of training samples	N	1 000 000
Density	ρ	Uniform on $[0.95, 1.05]$
Velocity magnitude	$ \mathbf{u} $	Uniform on $[0.00, 0.01]$
Std. deviation of non-eq. noise	σ_{neq}	Uniform on $[0.00, 5 \times 10^{-4}]$
Relaxation time	τ	1
Test split fraction	r_{split}	0.001

B. Optimal Circuit Architecture Experiments

Table 6: Training parameters used in the circuit architecture experiments.

Training Parameter	Setting
Optimizer	JAX Gradient Descent
Learning Rate	0.05
Training Iterations	250000
Batch Size	5
Momentum Conservation Penalty	Off
Accuracy Tolerance	1×10^{-5}
Parameter Initialization	Uniform on $[-\pi, \pi]$

C. SQC Depth Analysis Experiments

Table 7: Training parameters used in the circuit depth analysis experiments.

Training Parameter	Setting
Optimizer	JAX Gradient Descent
Learning Rate	0.05
Training Iterations	250000
Batch Size	5
Momentum Conservation Penalty	Off
Accuracy Tolerance	1×10^{-5}
Parameter Initialization	Uniform on $[-\pi, \pi]$

D. Momentum Loss Experiments

Table 8: Training parameters used in the momentum penalty experiments.

Training Parameter	Setting
Optimizer	JAX Gradient Descent
Learning Rate	0.05
Training Iterations	250000
Batch Size	5
Momentum Conservation Penalty	ON
Accuracy Tolerance	1×10^{-5}
Parameter Initialization	Uniform on $[-\pi, \pi]$